

The Paleocene-Eocene Thermal Maximum

Meissner, K. J.; Bralower, T. J.; Alexander, K.; Dunkley Jones, T.; Sijp, W.; Ward, M.

DOI:

[10.1002/2014PA002650](https://doi.org/10.1002/2014PA002650)

License:

None: All rights reserved

Document Version

Peer reviewed version

Citation for published version (Harvard):

Meissner, KJ, Bralower, TJ, Alexander, K, Dunkley Jones, T, Sijp, W & Ward, M 2014, 'The Paleocene-Eocene Thermal Maximum: how much carbon is enough?', *Paleoceanography*, vol. 29, no. 10, pp. 946-963.
<https://doi.org/10.1002/2014PA002650>

[Link to publication on Research at Birmingham portal](#)

Publisher Rights Statement:

Checked for eligibility: 15/01/2018

An edited version of this paper was published by AGU. Copyright 2014 American Geophysical Union.

Meissner, K. J., T. J. Bralower, K. Alexander, T. Dunkley Jones, W. Sijp, and M. Ward (2014), The Paleocene-Eocene Thermal Maximum: How much carbon is enough?, *Paleoceanography*, 19, 946–963, doi:10.1002/2014PA002650.

General rights

Unless a licence is specified above, all rights (including copyright and moral rights) in this document are retained by the authors and/or the copyright holders. The express permission of the copyright holder must be obtained for any use of this material other than for purposes permitted by law.

- Users may freely distribute the URL that is used to identify this publication.
- Users may download and/or print one copy of the publication from the University of Birmingham research portal for the purpose of private study or non-commercial research.
- User may use extracts from the document in line with the concept of 'fair dealing' under the Copyright, Designs and Patents Act 1988 (?)
- Users may not further distribute the material nor use it for the purposes of commercial gain.

Where a licence is displayed above, please note the terms and conditions of the licence govern your use of this document.

When citing, please reference the published version.

Take down policy

While the University of Birmingham exercises care and attention in making items available there are rare occasions when an item has been uploaded in error or has been deemed to be commercially or otherwise sensitive.

If you believe that this is the case for this document, please contact UBIRA@lists.bham.ac.uk providing details and we will remove access to the work immediately and investigate.

¹ **The Paleocene-Eocene Thermal Maximum:** ² **How much carbon is enough?**

K. J. Meissner¹⁻³, T. J. Bralower⁴, K. Alexander^{2,3}, T. Dunkley Jones⁵, W.
Sijp¹, M. Ward¹

K. J. Meissner, Climate Change Research Centre, University of New South Wales, Sydney,
2052, NSW, Australia (k.meissner@unsw.edu.au)

¹Climate Change Research Centre,
University of New South Wales, Australia

²ARC Centre of Excellence for Climate
System Science, Australia

³School of Earth and Ocean Sciences,
University of Victoria, Canada

⁴Department of Geosciences, The
Pennsylvania State University, USA

⁵School of Geography, Earth and
Environmental Science, University of
Birmingham, UK

3 The Paleocene-Eocene Thermal Maximum (PETM), ~ 55.53 million years
4 before present, was an abrupt warming event that involved profound changes
5 in the carbon cycle and led to major perturbations of marine and terrestrial
6 ecosystems. The PETM was triggered by the release of a massive amount
7 of carbon, and thus the event provides an analogue for future climate and
8 environmental changes given current anthropogenic CO₂ emissions. Previ-
9 ous attempts to constrain the amount of carbon released have produced widely
10 diverging results, between 2000 and 10 000 gigatonnes carbon (GtC). Here
11 we use the UVic Earth System Climate Model in conjunction with a recently
12 published compilation of PETM temperatures [*Dunkley Jones et al.*, 2013]
13 to constrain the initial atmospheric CO₂ concentration as well as the total
14 mass of carbon released during the event. Thirty-six simulations were ini-
15 tialized with varying ocean alkalinity, river runoff, and ocean sediment cover.
16 Simulating various combinations of pre-PETM CO₂ levels (840, 1680, and
17 2520 ppm) and total carbon releases (3000, 4500, 7000, and 10 000 GtC),
18 we find that both the 840 ppm plus 7000 GtC and 1680 ppm plus 7000-10000
19 GtC scenarios agree best with temperature reconstructions. Bottom waters
20 outside the Arctic and North Atlantic Oceans remain well oxygenated in all
21 of our simulations. While the recovery time and rates are highly dependent
22 on ocean alkalinity and sediment cover, the maximum temperature anomaly,
23 used here to constrain the amount of carbon released, is less dependent on
24 this slow acting feedback.

1. Introduction

The Paleocene-Eocene Thermal Maximum (PETM), ~ 55.53 million years before present [Westerhold *et al.*, 2007], is arguably the most intensively studied abrupt warming event in the geologic record (e.g., Kennett and Stott [1991]; Dickens *et al.* [1995]; Thomas and Shackleton [1996]; Thomas *et al.* [2002]; Zachos *et al.* [2003, 2005]; Sluijs *et al.* [2007a]). Thousands of gigatonnes (Gt) of carbon were released into the atmosphere and ocean over less than 20 000 years leading to profound changes in climate, the carbon cycle, and ocean chemistry, as well as major perturbations in marine and terrestrial ecosystems (e.g. Kelly *et al.* [1996]; Dickens *et al.* [1997]; Sloan and Thomas [1998]; Thomas [1998]; Bains *et al.* [1999]; Crouch *et al.* [2001]; Bralower [2002]; Wing *et al.* [2005]; see Sluijs *et al.* [2007b] and McInerney and Wing [2011] for thorough reviews). The event is of particular interest because it may provide an analogue for future climate and environmental change if anthropogenic CO₂ emissions continue on their current trajectory (e.g., Ridgwell and Schmidt [2010]; Zeebe and Zachos [2013]).

The PETM is associated with substantial warming of sea surface and deep waters, based on interpretation of several proxies: oxygen isotopes and Mg/Ca ratios measured in foraminifera and the lipid-based TEX₈₆ proxy [Kennett and Stott, 1991; Thomas and Shackleton, 1996; Thomas *et al.*, 2002; Zachos *et al.*, 2003; Sluijs *et al.*, 2007a]. Reconstructed temperatures show a significant amount of variation resulting from proxy discrepancies, local environmental effects and foraminiferal recrystallization (e.g. Bralower *et al.* [1995]; Zachos *et al.* [2003]; Kozdon *et al.* [2013]). Recently Dunkley Jones *et al.* [2013] compiled and compared the available temperature data and assessed the reliability

of proxy temperature estimates. They estimated the global mean surface temperature anomaly to be within the range of 4 to 5°C and the intermediate water temperature anomaly to be ~5°C.

Although the PETM has received vigorous study by the paleoclimate community, the pre-existing climate and the magnitude of the perturbation remain poorly resolved. For example, late Paleocene (pre-PETM) atmospheric CO₂ concentration estimates vary widely. *Pearson and Palmer* [2000] found late Paleocene concentrations exceeding 2400 ppm based on boron-isotope ratios of planktonic foraminiferal shells. This is in stark contrast with estimates of concentrations below 300 ppm and 400 ppm, based on modeled carbon isotope gradients [*Hilting et al.*, 2008] and leaf stomatal indices [*Royer et al.*, 2001], respectively. A recent study by *Schubert and Jahren* [2013] constrained the range of late Paleocene carbon dioxide concentrations to 674-1034 ppm. Since the radiative forcing of an atmospheric CO₂ change depends on the background concentration, a given release of carbon will cause more warming in a low-CO₂ atmosphere than in a high-CO₂ atmosphere. In other words, the higher the initial CO₂ concentration, the larger the carbon release that is required to explain the same amount of warming. A better understanding of pCO₂ levels immediately before the PETM is therefore essential in order to reconstruct the event itself.

Estimates of the total amount of carbon released during the PETM also vary significantly. *Zachos et al.* [2005] estimated a total release of > 4500 GtC based on the extent of sea-floor carbonate dissolution. *Panchuk et al.* [2008] refined this number to > 6800 GtC, based on dissolution estimates simulated with the GENIE-1 model. Reconstruction

of Arctic hydrology also supported the high release estimate [Pagani *et al.*, 2006a]. At the other end of the spectrum, Zeebe *et al.* [2009] constrained the initial carbon release to < 3000 GtC, based on simulations of carbonate dissolution and the magnitude of the carbon isotope excursion using the carbon cycle model LOSCAR. More precise estimates of the magnitude and rate of carbon release are vital to determine the source of CO_2 that fueled the PETM (e.g. Dickens *et al.* [1997]; Kurtz *et al.* [2003]; Panchuk *et al.* [2008]), to understand the magnitude of potential positive feedbacks in the natural climate system during the event, and to constrain changes in ocean chemistry and marine and terrestrial ecosystems resulting from future anthropogenic CO_2 emissions.

The lack of consensus on the background CO_2 levels and the magnitude of the carbon pulse necessitates an independent approach. Here, we use a climate model of intermediate complexity (the UVic Earth System Climate Model [Weaver *et al.*, 2001]) in conjunction with a recently published compilation of temperature reconstructions [Dunkley Jones *et al.*, 2013] to constrain the atmospheric CO_2 concentration prior to the PETM as well as the amount of carbon released during the event.

2. Methods

The UVic Earth System Climate Model (UVic ESCM) consists of an ocean general circulation model (Modular Ocean Model, Version 2, [Pacanowski, 1995]) coupled to a vertically integrated two dimensional energy-moisture balance model of the atmosphere, a dynamic-thermodynamic sea ice model, a land surface scheme, a dynamic global vegetation model [Meissner *et al.*, 2003], and a sediment model [Archer, 1996; Meissner *et al.*, 2012]. It also includes a fully coupled carbon cycle [Matthews *et al.*, 2005; Meissner

89 *et al.*, 2003; *Schmittner et al.*, 2008]. The marine ecosystem/biogeochemical model is an
90 improved NPZD (nutrient, phytoplankton, zooplankton, detritus) model with a param-
91 eterization of fast nutrient recycling due to microbial activity [*Schartau and Oschlies*,
92 2003]. It includes two phytoplankton classes (nitrogen fixers and other phytoplankton),
93 one zooplankton class, two nutrients (nitrate and phosphate), oxygen, dissolved inorganic
94 carbon and alkalinity as prognostic tracers. Carbonate production is calculated as a fixed
95 proportion of primary production, which is indirectly a function of temperature through
96 the Eppley function [*Eppley*, 1972]. A complete description of the ecosystem model can
97 be found in *Schmittner et al.* [2008]. The ocean biogeochemical model calculates carbon
98 fluxes to the sediments as well as their rain ratios. Sediment processes are represented
99 using a model of deep ocean sediment respiration [*Archer*, 1996; *Meissner et al.*, 2012].
100 This model assumes oxic conditions, therefore all incoming organic carbon is assumed to
101 dissolve. The remaining CaCO_3 is added to the first sediment layer, eventually passes
102 through the pore layers to be added to more stable layers and finally the lithosphere.
103 Weathering fluxes are either based on atmospheric CO_2 concentrations or a combination
104 of surface atmospheric temperature and net primary productivity [*Meissner et al.*, 2012].
105 The UVic ESCM is computationally very efficient and has been developed to address
106 scientific questions related to climate variability on time scales of hundreds of years to
107 millennia (e.g. *Meissner et al.* [2008]; *Eby et al.* [2009]).

108 For the present study, we integrated four control simulations for over 10 000 years
109 with Eocene paleogeography, bathymetry and wind fields [*Sijp et al.*, 2011]. Orbital
110 parameters and the solar constant were set to present day values. Simulations were

integrated with atmospheric CO₂ concentrations held constant at 280, 840, 1680 and 2520 ppm. The three warmer simulations were then forced with carbon emission pulses of 3000, 4500, 7000 and 10 000 GtC over one year. While pulse scenarios are commonly used in the modelling community for simplicity and ease of comparison between models (e.g., *Cao et al.* [2009]; *Eby et al.* [2009]), they likely overestimate the short-term temperature and atmospheric carbon dioxide response. Recently *Wright and Schaller* [2013] proposed that the PETM was indeed triggered by an instantaneous release based on proxy and sedimentary data, but this interpretation has been disputed (e.g., *Zeebe et al.* [2014]). The long-term climate response appears to be independent of the rate at which CO₂ is emitted (e.g., *Eby et al.* [2009]; *Meissner et al.* [2012]). In addition, one set of gradual release scenarios was integrated with emissions of 1 GtC per year for 4500 years to simulate a slower release scenario (e.g. *Cui et al.* [2011]). Each scenario was integrated twice with differing weathering parameterizations [*Meissner et al.*, 2012], based on either a combination of surface atmospheric temperature and net primary productivity [*Lenton and Britton*, 2006] or on atmospheric CO₂ concentrations [*Zeebe et al.*, 2008], termed LB and ZL hereafter (see Table 1 for a list of all simulations).

During model spin-up, total alkalinity and DIC are conserved by balancing sedimentary CaCO₃ deposition with the alkalinity and DIC fluxes from river discharge [*Meissner et al.*, 2012]. Calcium and magnesium ion concentrations are assumed constant and equal to modern concentrations when solving for saturation state. Sediments, ocean biogeochemistry and the global carbon cycle then adjust to the given pre-defined global mean ocean alkalinity. During transient simulations, the weathering fluxes are calculated prog-

133 nostically and global alkalinity and DIC are free to evolve. Figure 1a-c shows the model
134 percent dry weight CaCO_3 at the end of the three warmer control simulations integrated
135 with present day global mean ocean alkalinity (2.429 mol/m^3). Sediment cover is low
136 in these high- CO_2 scenarios, which likely leads to an underestimation of the sediment-
137 alkalinity feedback during the recovery period. To address this issue, we integrated three
138 additional control simulations with 1680 ppm CO_2 and global mean alkalinity increased
139 by a factor of 2 (4.858 mol/m^3 , 1680_Alk2), 1.5 (3.644 mol/m^3 , 1680_Alk15), and 1.2
140 (2.915 mol/m^3 , 1680_Alk12). Simulated percent dry weight CaCO_3 at the end of these
141 simulations is shown in Figure 1d, 1e, 1f, and 1b respectively; the global mean equals 77%
142 (1680_Alk2), 44% (1680_Alk15), 19% (1680_Alk12) and 7% (1680). Each high-alkalinity
143 simulation was then forced with a carbon emission pulse of 7000 GtC. 1680_Alk15 was
144 also forced with pulses of 3000, 4500, and 10000 GtC (Table 1).

145 Model results were compared to a compilation of SST and deep water temperature
146 estimates for the interval immediately preceeding the PETM and the peak of the event
147 [*Dunkley Jones et al.*, 2013]. The compilation includes estimates based on $\delta^{18}\text{O}$, Mg/Ca
148 and TEX_{86} temperature proxies.

3. Results

3.1. Late Paleocene climate conditions

149 All six equilibrium simulations form deep water in the North Pacific, while there is
150 little to no deepwater formation in the North Atlantic. In all simulations Southern Ocean
151 sourced bottom water is the dominant water mass (similar to earlier studies, e.g. *Bice and*
152 *Marotzke* [2001]; *Thomas et al.* [2003]; *Winguth et al.* [2012]), and the Tethys Ocean forms

153 warm and saline deep water which sinks to a depth of $\sim 1000\text{m}$. Figure 2 shows simulated
154 annual sea surface temperatures (SSTs) together with reconstructed SSTs compiled by
155 *Dunkley Jones et al.* [2013] at Deep Sea Drilling Project (DSDP) Site 527, Ocean Drilling
156 Program (ODP) Sites 690, 865, 1172 and 1209, and Leg 174AX Bass River and Wilson
157 Lake cores from on-shore New Jersey, and Integrated Ocean Drilling Program (IODP)
158 Leg 302 ACEX Core 4A from the Lomonosov Ridge (Arctic Ocean). Where multiple
159 proxies exist at a single site, the median SST was plotted. Figure 3a shows all pre-
160 PETM temperature proxies along with estimates for proxy calibration uncertainty and
161 one standard deviation of data variability (see *Dunkley Jones et al.* [2013] for details).

162 From both figures it is clear that none of our simulations is able to reproduce the warm
163 SST proxy interpretations at the high-latitude ACEX core (tagged with [1] in Figure 2a)
164 and Site 1172 [8]. The warmer simulations (840 ppm, 1680 ppm and 2520 ppm) are all
165 three in agreement with the third high-latitude Site 690 [7] as well as with the mid-latitude
166 cores Bass River [2] and Wilson Lake [3]. Sites 1209 [4] and 865 [5] in the tropics align
167 best with the 840 ppm simulation, whereas SSTs from Site 527 [6] in the South Atlantic
168 are consistent with the two warmest simulations (1680 ppm and 2520 ppm).

169 We quantified the model-proxy disparity for each site as the absolute difference between
170 modelled SST (interpolated to the correct location) and the closest proxy reconstruction.
171 If modelled SST fell within the error bounds of a proxy, the disparity was defined as
172 0. Figure 3b shows this metric plotted for each core. Other than for the previously
173 discussed high-latitude ACEX core [1] and Site 1172 [8], the three warmer simulations
174 always achieve a model-proxy disparity below 2.5°C . Given that the proxy data themselves

175 present important discrepancies for a given site, we calculate the median disparity (which
176 by definition gives less weight to outliers than the mean disparity) to establish which
177 control simulation is closest to reconstructions. Overall, the median disparity across all
178 proxies is lowest for the 840 ppm simulation at 0°C. Simulation 1680 has the second lowest
179 median disparity (0.025°C). Thus either the 840 or 1680 ppm simulations are plausible,
180 especially if pre-PETM $\delta^{18}\text{O}$ proxies are regarded as minimum estimates [*Dunkley Jones*
181 *et al.*, 2013].

182 When we calculate the model-proxy disparity for each proxy separately, we find that
183 both $\delta^{18}\text{O}$ and Mg/Ca proxy SSTs agree best with the 840 ppm simulation (median
184 disparities of 0°C); TEX proxy SSTs are closest to the 2520 ppm simulation (median
185 disparity 1.8°C). Although the calculation of Mg/Ca-based temperatures relies on various
186 assumptions about seawater Mg/Ca, the calibrations used best-fit independent estimates
187 of Mg/Ca_{sw} and are in reasonable agreement with $\delta^{18}\text{O}$ -derived temperatures from sites
188 with excellent planktic foraminiferal preservation (see discussion in *Dunkley Jones et al.*
189 [2013]). For the $\delta^{18}\text{O}$ proxy-based disparity calculation, we disregarded oxygen isotope data
190 from Sites 527, 865 and 1209 based on the large discrepancy between $\delta^{18}\text{O}$ and Mg/Ca
191 temperatures on the order of $\sim 10^\circ\text{C}$ [*Dunkley Jones et al.*, 2013]. The median disparity
192 across all proxies is not affected by the inclusion of $\delta^{18}\text{O}$ from these three sites.

193 Other than Sites 865 and 1051 (both at $\sim 1500\text{m}$ depth) and the Bass River and Wil-
194 son Lake cores (both $< 150\text{m}$ deep [*Harris et al.*, 2010]), bottom water temperatures are
195 underestimated in all simulations when compared to proxy estimates (Figure 3c). Cali-

196 bration uncertainty for benthics is shown as $\pm 1^\circ\text{C}$ for both Mg/Ca [*Lear et al.*, 2002] and
197 $\delta^{18}\text{O}$ [*Kim and O'Neil*, 1997].

3.2. The carbon pulse

198 Time series for atmospheric carbon anomalies show that the two weathering schemes
199 yield very similar results, especially when initialized with the warmest climate (2520
200 ppm, Figure 4, compare dotted lines with solid lines). Even with a colder initial climate
201 (840 ppm) the two weathering schemes show less discrepancy in the recovery than when
202 integrated under present day conditions [*Meissner et al.*, 2012]. As expected, temperature
203 response decreases with increasing background CO_2 , for example a 10 000 GtC pulse has
204 a larger impact on temperature for the 840 ppm simulations than for the 2520 ppm
205 simulations. Global mean ocean temperatures take over 5000 years to equilibrate. There
206 is little to no recovery in atmospheric CO_2 and temperatures during the 10 000 years of
207 integration for simulations that started with present day global mean alkalinity, indicating
208 that the climate system is so saturated in CO_2 that the land and ocean can absorb little of
209 the excess atmospheric carbon. Simulations with higher ocean alkalinity (dashed lines in
210 Figure 4, middle panels) show a significantly faster recovery in atmospheric CO_2 , especially
211 for high emissions (7000 and 10 000 GtC). While the maximum increase in surface air
212 temperature is similar for simulations that started with different alkalinities, deep ocean
213 warming is slightly less for higher alkalinity simulations (Figure 4e and h).

214 All 36 simulations indicate an initial decrease in global mean oceanic oxygen concentra-
215 tions followed by a recovery (last row of Figure 4). Figure 5 (first row) shows the values of
216 vertical minimum oxygen concentrations in hypoxic regions during the 840, 1680, and 2520

217 ppm control simulations. While there is widespread hypoxia (defined here as regions with
218 oxygen concentrations below $90\mu\text{M}$) in the tropics in all simulations, the Arctic and parts
219 of the Southern Ocean become hypoxic for higher atmospheric CO_2 concentrations. Most
220 of these hypoxic regions are located within the uppermost 1000m of the water column
221 (Figure 5e). Only the Arctic Ocean as well as some continental shelves in the Atlantic
222 Ocean experience bottom-water oxygen levels below $30\mu\text{M}$ during the most oxygen de-
223 pleted simulation (2520_10000_LB, Figure 5f). The bottom water of the Atlantic Ocean
224 is also depleted but stays above $60\mu\text{M}$ during this simulation.

225 Sediment chemistry timeseries are shown in Figure 6. The percentage of calcite in
226 sediments increases during the first several thousand years in all simulations (Figure 6,
227 third row). This is due to a temperature-driven increase in global mean photosynthesis and
228 calcite production (see detailed discussion in *Meissner et al.* [2012]), which compensates
229 for the initial increase in dissolution in sediments (Figure 6, first and second rows) and acts
230 as a weak positive feedback on atmospheric CO_2 concentrations. After several thousand
231 years, the acidification signal of the carbon pulse reaches the deep ocean (note the steeper
232 increase in dissolution: Figure 6, second row). Dissolution exceeds the downward flux of
233 calcite and the total mass of calcite in the pore layer decreases. The last row in Figure 6
234 shows the change in the global mean calcite compensation depth (diagnosed here as the
235 mean depth of grid boxes with less than 10% dry weight CaCO_3). A temporary shoaling
236 of this metric can be seen for all simulations.

237 Figure 7 shows the simulated maximum SST anomalies at the eight sites compared
238 to proxy reconstructions. While the reconstructions often exhibit considerable spread,

there is some overlap with the simulations at nearly all sites. Note that proxy data from Sites 865 [5] and 527 [6] likely underestimate the temperature anomaly for stratigraphic reasons (chemical erosion or “burndown” of the basal few thousand years of the PETM, *Dunkley Jones et al.* [2013]). Proxy reconstructions for all other sites are compatible with the high emission scenarios (7000-10000 Gt C) especially when started with a higher CO₂ background climate of 1680 or 2520 ppm.

Maximum proxy bottom water temperature anomalies are shown in Figure 8, with depth ranging from 80m (Wilson Lake, first panel) to 3400m (DSDP 527, last panel). Bottom temperature proxies from Site 1209 [4] show a small peak increase compared to most simulations and proxy data from all other sites, which might be due to chemical erosion and/or slow deposition rates [*Dunkley Jones et al.*, 2013]. Bottom temperature proxy reconstructions for other sites agree best with the higher emission scenarios.

The median model-proxy disparity for sea surface temperature anomalies is minimized for three distinctive scenarios: a low-carbon scenario (initial CO₂ of 840 ppm plus a carbon forcing of 4500 GtC; overall median disparity of 0.348°C); a medium scenario (1680 ppm + 7000 GtC, median disparity 0.133°C); and a high-carbon scenario (2520 ppm + 10000 GtC, median disparity 0.20°C). One should bear in mind that the design of our model simulations (emission pulse over one year) tends to overestimate the surface temperature response. Furthermore, the proxy data in several deep sea sites are likely to have missed the peak temperature because of chemical erosion or low temporal resolution. We therefore conclude that based on SST anomalies, the carbon pulse was likely 7000-10000 Gt C or higher. When analyzing bottom temperatures, the minimum model-proxy disparities are

261 achieved for slightly more carbon intensive scenarios: 840 ppm + 7000 GtC (0.362°C);
262 1680 ppm + 10 000 GtC (0.67°C); and 2520 ppm + 10 000 GtC (1.197°C). Overall, the
263 amount of released carbon required to cause the reconstructed temperature anomalies
264 depends heavily on the initial atmospheric carbon dioxide concentration: 7000 GtC for
265 pre-PETM atmospheric CO₂ concentrations of 840 ppm; 7000-10 000 GtC for pre-event
266 CO₂ concentrations of 1680 ppm and over 10 000 GtC for pre-PETM atmospheric CO₂ of
267 2520 ppm.

4. Discussion

268 Previous model-based estimates of the magnitude of the carbon perturbation required
269 to trigger the PETM were constrained by the size of the carbon isotope excursion or the
270 extent of deep ocean dissolution (e.g., *Panchuk et al.* [2008]). The results show consider-
271 able variation due to the range of complexity of the models used as well as the unknown
272 background chemistry of Paleocene ocean water. To refine our understanding of PETM
273 atmospheric forcing, we apply a novel model-data combination: the UVic model which
274 was built for long-term simulations with a special focus on ocean dynamics and feedbacks
275 [*Weaver et al.*, 2001] and a recently published compilation of proxy surface and deep water
276 temperature data [*Dunkley Jones et al.*, 2013]. Here we interpret the results and impli-
277 cations of the model-data comparison beginning with a discussion of the uncertainties of
278 the data and the sensitivity of model simulations, followed by a comparison of the results
279 with those of previous investigations.

4.1. Uncertainties in proxy data reconstructions

Investigation of a climate event that took place 55 million years ago is fraught with challenges, both for modelling and proxy analysis. Deep ocean acidification resulting from the carbon release led to widespread dissolution of the carbonate microfossils which were deposited during and immediately before the PETM at deep sea sites [*Zachos et al.*, 2005; *Colosimo et al.*, 2006; *Zachos et al.*, 2007; *Murphy et al.*, 2010]; thus precise constraint of the peak warming signal is not possible at these locations. Oxygen isotope variations across the PETM are impacted by changes in salinity as well as temperature. In tropical sites, for example, an increase in evaporation is thought to have decreased the amplitude of the temperature signal [*Zachos et al.*, 2003]; conversely, fresh water input at high-latitude Site 690 may have increased the amplitude. The Mg/Ca values of seawater are known to change through time and temperature estimates based on them rely heavily on the calibration applied (e.g., *Evans and Müller* [2012]). Interpretation of Mg/Ca and particularly $\delta^{18}\text{O}$ values is also confounded by possible alteration of carbonate microfossils during burial. Carbonate recrystallization decreases the magnitude of the PETM SST increase, especially at low-latitude deep-sea sites (e.g., *Pearson et al.* [2001]). GDGT lipid-based proxies, used in coastal and high-latitude PETM sections, circumvent such diagenetic issues but are subject to significant calibration uncertainty, especially during warm climate states (e.g., *Kim et al.* [2010]; *Hollis et al.* [2012]) and with changing productivity regimes [*Taylor et al.*, 2013]. For a more detailed discussion of the uncertainties within the pre-PETM and PETM proxy data set see *Dunkley Jones et al.* [2013].

4.2. Uncertainties in major ion seawater composition

300 Model simulations rely heavily on boundary conditions, which have significant uncer-
301 tainties during this period. Topography and wind forcing, in particular, are major un-
302 knowns which greatly influence the climate state. Little is known about the orbital pa-
303 rameters or the background chemistry (pre-PETM ocean alkalinity [*Cui et al.*, 2011]). For
304 example, *Lowenstein et al.* [2001] suggest that the $\text{Mg}^{2+}/\text{Ca}^{2+}$ ratio increased from <2.3
305 in the Cretaceous to >2.5 between 50 and 0 Ma. The Ca^{2+} concentration in seawater is
306 believed to have reached maximum values two to three times greater than modern values
307 in the Cretaceous and was also likely higher during the Eocene than today (*Horita et al.*
308 [2002], their Figure 8). The major ion composition is crucial for calculating seawater
309 chemistry, saturation and the capacity of carbon uptake by the ocean [*Tyrrell and Zeebe*,
310 2004]. However, Ocean General Circulation Models (OGCMs) do not generally include
311 sophisticated seawater chemistry models. In the group of climate models including full
312 ocean GCMs, the UVic model has one of the most detailed biogeochemistry components.
313 While we cannot take variations in the concentrations of any particular major seawater
314 ion into account, we can vary the global mean ocean alkalinity as a measure of carbonate
315 and bicarbonate ions in the ocean. Figure 1b and d show two extreme cases of background
316 alkalinity and their impact on ocean sediments. The percent dry weight CaCO_3 in the
317 late Paleocene was probably between these two extremes [*Panchuk*, 2007], which gives
318 us confidence that our simulations have spanned the parameter space of possible climate
319 responses to a certain carbon pulse (including climate sensitivity) with regard to initial
320 marine sediment cover [*Goodwin et al.*, 2009; *Goodwin and Ridgwell*, 2010]. While the
321 long-term recovery of atmospheric CO_2 is highly dependent on the initial alkalinity and

sediment cover (Figure 4, middle panels), the maximum temperature response acts on much shorter timescales (especially for surface temperatures) and is less influenced by the background ocean chemistry.

4.3. Climate sensitivity

The climate sensitivity of the UVic Earth System Climate Model is a key parameter for the analysis presented here. Climate sensitivity is often split into fast feedbacks (e.g. water vapor, snow albedo, sea ice albedo; also called the ‘Charney sensitivity’) and slow feedbacks (e.g. vegetation, ice sheets, ocean circulation). While the IPCC 2013 report states that the Charney sensitivity “is likely in the range 1.5°C to 4.5°C (high confidence), extremely unlikely less than 1°C (high confidence), and very unlikely greater than 6°C (medium confidence)” [Stocker *et al.*, 2013], these values have been challenged in the past, especially for warmer background climates [Pagani *et al.*, 2010; Lunt *et al.*, 2010]. Based on a sensitivity study of the Pliocene Lunt *et al.* [2010] suggest a 30-50% higher climate sensitivity due to slow feedbacks not included in coupled GCMs. It should be noted, however, that their model does not include the sediment-alkalinity or weathering feedbacks, which are the main negative slow feedbacks in the climate system. In a more recent paper, Rohling *et al.* [2013] revisit climate sensitivity over the past 65 million years and find values which agree with the most recent IPCC report [Stocker *et al.*, 2013]. On the other hand, Schmittner *et al.* [2011] find that modern climate models are more likely to over- than to under-estimate climate sensitivity; a view that has been challenged recently [Fyke and Eby, 2012]. Cloud feedbacks, a significant source of uncertainty in future climate projections, are particularly poorly understood under CO₂ concentrations four to nine

times preindustrial values [Abbot and Tziperman, 2009; Kiehl and Shields, 2013]. Lunt *et al.* [2012] find that the main reasons for differences between early Eocene simulations by five different models include differences in surface albedo feedbacks, water vapor and lapse rate feedbacks, as well as prescribed aerosol loading, rather than differences in cloud feedbacks.

The simulations presented here show the reaction of the climate system to a carbon pulse within the first 10 000 years of the PETM. The UVic model includes the classic Charney feedbacks in addition to some of the slower feedbacks (e.g., vegetation, alkalinity, ocean circulation, weathering fluxes). With these feedbacks, the UVic ESCM has a climate sensitivity of 3.3°C under PETM boundary conditions, which is slightly lower than under preindustrial boundary conditions (3.5°C, *Weaver et al.* [2007]) and which falls within the range suggested by the IPCC and *Rohling et al.* [2013].

4.4. High latitude temperatures and meridional temperature gradient

The latitudinal temperature gradient at the surface is slightly overestimated in our simulations compared to temperature reconstructions (Figure 2). This might be partially due to a potential underestimation of low-latitude SSTs by proxy data (e.g. *Huber* [2008]). However, the UVic model clearly faces the well-known problem of climate models simulating polar regions that are too cool in high-CO₂ climates (e.g. *Sloan and Barron* [1990]; *Heinemann et al.* [2009]; *Huber and Caballero* [2011]; *Valdes* [2011]; *Lunt et al.* [2012]; *Sagoo et al.* [2013]). All of our equilibrium model simulations fail to capture warm temperatures suggested by proxy data from two of the three high-latitude locations: the ACEX site [1] and Site 1172 [8] (Figure 3a and b), from the Arctic and Southern Oceans,

364 respectively. The extremely high temperatures reconstructed in ACEX are particularly
365 puzzling. Our simulations show the Arctic Ocean to be largely isolated, with high river
366 runoff and precipitation exceeding evaporation, leading to very fresh and stratified wa-
367 ters. These conditions are in agreement with salinity proxies and fossil assemblages [*Sluijs*
368 *et al.*, 2006; *Waddell and Moore*, 2008]. The surface water masses are therefore in close
369 thermal equilibrium with the overlying atmosphere, with almost no heat exchange with
370 deeper layers or other ocean basins. Consequently, the reconstructed high temperatures
371 in the Arctic could have only been achieved by locally increased longwave radiation (e.g.
372 polar stratospheric clouds [*Sloan and Pollard*, 1998], or changes in cloud condensation
373 nuclei [*Kiehl and Shields*, 2013]), locally changed short wave radiation (e.g. obliquity, *Se-*
374 *wall and Sloan* [2004]) or more efficient heat transport in the atmosphere (stronger winds
375 and/or increase in latent heat transport).

376 Site 1172 [8] in the Pacific sector of the Southern Ocean records higher temperatures
377 than Site 690 [7], which is at a similar latitude but in the Atlantic sector. A possible
378 explanation for the warm proxy temperature estimates at Site 1172 given its location
379 on the east coast of Australia, involves southward shifted westerlies concurrent with an
380 intensified western boundary current, which would transport warm low-latitude waters
381 further south than in our simulations. It is also possible that GDGT-based proxies are
382 over-estimating SSTs at high-latitude locations, such as Site 1172 and the ACEX site
383 (e.g., *Hollis et al.* [2012]; *Taylor et al.* [2013]), or that a seasonal bias of the proxies is
384 causing additional model-data disagreement [*Lunt et al.*, 2012].

385 Bottom water temperatures in all simulations are underestimated in two-thirds of the
386 sites considered (Figure 3c). Given that bottom temperatures reflect conditions at deep
387 water formation sites, the model's underestimation of bottom water temperatures and
388 overestimation of surface temperature gradient are likely connected. Although there is
389 significant deep water formation in the Tethys Ocean, this water mass is not dense enough
390 to significantly influence deep water circulation patterns. Therefore, our model does not
391 support the long-since-refuted WSBW (warm saline bottom water) hypothesis (*Bice and*
392 *Marotzke* [2001] and references therein).

4.5. Temperature versus dissolution

393 Previous estimates of carbon input are based on simulations of deep ocean dissolution
394 [*Panchuk et al.*, 2008; *Zeebe et al.*, 2009; *Cui et al.*, 2011]. Our simulations were not
395 integrated long enough to capture the full dissolution event (Figure 6). While the UVic
396 model is better skilled at simulating ocean dynamics and changes in three-dimensional
397 temperature fields than most other climate models of intermediate complexity, it is compu-
398 tationally too intensive to allow for long enough integrations to analyze maximum changes
399 in the calcite compensation depth. Furthermore, there are two additional uncertainties
400 to consider when analyzing modelled changes in the calcite compensation depth. First,
401 deep ocean dissolution depends on background seawater ion concentration (Section 4.2,
402 Figures 1 and 6) and would therefore require a range of long-term simulations spanning
403 the parameter space of alkalinity [*Cui et al.*, 2011]. Second, it is still debated how calcite
404 production and export react to increasing atmospheric CO₂, with models showing both
405 an increase and decrease in export [*Gehlen et al.*, 2007; *Ridgwell et al.*, 2007; *Schmittner*

406 *et al.*, 2008; *Meissner et al.*, 2012]. In addition, the stratigraphic record of the earliest
407 part of the PETM at many of the study sites is compromised by chemical erosion. Given
408 these model and stratigraphic complications, we do not interpret the apparent mismatch
409 between the modelled CaCO_3 results and percentages in the study sections.

4.6. How much CO_2 is enough?

410 The estimate of the amount of carbon required to generate PETM warming depends
411 heavily on the pre-PETM carbon dioxide concentrations [*Pagani et al.*, 2006b]. Estimates
412 of late Paleocene atmospheric CO_2 concentrations range widely from 200 ppm to 2800 ppm
413 (*McInerney and Wing* [2011] and references therein). Here we find that simulated SSTs
414 agree best with temperature reconstructions for atmospheric CO_2 concentrations between
415 840 and 1680 ppm, while the best fit between model and data in terms of sediment cover
416 is achieved for an atmospheric CO_2 concentration of 1680 ppm and global mean ocean
417 alkalinity of 3.644 mol/m^3 (not shown). Further, proxy data and model simulations fit
418 best with either a low-carbon scenario (pre-PETM atmospheric CO_2 of 840 ppm plus a
419 carbon release of 4500-7000 GtC), a medium scenario (1680 ppm plus 7000-10 000 GtC)
420 or a high-carbon scenario (2520 ppm plus $> 10\,000$ GtC).

421 While a release of 4500 GtC agrees with earlier estimates based on the shoaling of
422 the calcite compensation depth [*Zachos et al.*, 2005; *Zeebe et al.*, 2009], it underesti-
423 mates bottom temperature anomalies in our study unless pre-PETM CO_2 concentrations
424 were below 840 ppm. However, 840 ppm is the minimum CO_2 concentration required to
425 achieve pre-event reconstructed temperatures. Given that the design of our simulations
426 (pulse emission) entails an overestimation of maximum simulated temperature anoma-

lies, both pre-PETM atmospheric CO₂ concentrations and total release are likely to be conservative estimates. Furthermore, our simulations with modern background alkalinity likely overestimate the deep ocean temperature response and hence also underestimate the total release of carbon. Our study therefore agrees with *Pagani et al.* [2006a]’s climate sensitivity-based estimate (> 5400 GtC) and *Panchuk et al.* [2008]’s simulations based on the extent of seafloor CaCO₃ dissolution (> 6800 GtC). Our high-carbon scenario is also in line with *Cui et al.* [2011]’s *C_{org}* scenario, who forced the GENIE model with a prescribed atmospheric $\delta^{13}\text{C}$ (13 000 GtC).

4.7. Deep-sea anoxia

All three of our best-fit simulations are consistent with a bottom water temperature increase of 4-5 °C (Figure 4) without a significant change in thermohaline circulation patterns, corroborating the study of *Thomas et al.* [2003]. While annual and global mean export production decreases by up to 20% in our simulations (not shown), overall the combination of warmer ocean temperatures and reduced ventilation leads to an expansion of hypoxic regions (Figure 5), a finding that has been observed in paleoredox proxies [*Chun et al.*, 2010]. The Arctic Ocean becomes almost entirely hypoxic in our high CO₂ simulations, due to a very stratified water column. Other than in the Arctic Ocean and the deep North Atlantic Ocean, hypoxic regions are situated within the first 1000-1500m of the water column. This is in contrast to *Winguth et al.* [2012] who found widespread dysoxia in bottom waters in a 2500 year long simulation with CCSM3 under 4480 ppm. While their simulations with the CCSM3 model were integrated under higher atmospheric CO₂ forcing than our simulations, their integration time of 2500 years was rather short

to equilibrate deep ocean temperatures and the associated vertical temperature gradient and stratification; the stratification in *Winguth et al.* [2012]’s simulations might therefore be overestimated. On the other hand, the UVic ESCM is missing wind-climate feedbacks which can influence upwelling and nutrient availability and therefore export production and deep-sea oxygen. The simulated deep-sea oxygen might also be overestimated because of the negative bias in simulated bottom water temperatures (Figure 3c). Observation of suboxia in the deep North Atlantic is consistent with *Pälike et al.* [2014] who found that Atlantic intermediate waters were suboxic during the PETM but those from the Pacific were not.

5. Conclusions

Estimates of late Paleocene atmospheric CO₂ concentrations and the magnitude of the PETM carbon release vary widely in the literature. Here we take advantage of a recently published compilation of recalculated paleotemperatures [*Dunkley Jones et al.*, 2013] to independently determine these variables using the UVic Earth System Climate Model. We integrated thirty-six 10 000-year long simulations under varying PETM boundary conditions. We find three scenarios that best align with proxy reconstructions of PETM temperature anomalies: a low-carbon scenario (late Paleocene atmospheric CO₂ concentration of 840 ppm and a PETM carbon pulse of 7000 GtC), a medium-carbon scenario (1680 ppm and 7000-10 000 GtC) and a high-carbon scenario (2520 ppm and > 10 000 GtC). The low- and medium-carbon scenarios fit best with pre-PETM absolute temperature reconstructions. However, the number of locations for which we have reliable SST reconstructions is small, and the reconstructed temperatures at each of these locations

469 varies widely depending on the proxy and species used. Furthermore, several important
470 boundary conditions for the modelling study are highly uncertain (alkaline run-off from
471 rivers [Cui *et al.*, 2011], topography, and clouds). Ocean bottom waters remain well
472 oxygenated in all our simulations other than for the Arctic and North Atlantic Oceans.

473 **Acknowledgments.** We would like to thank Christopher Charles as well as four anony-
474 mous reviewers for their helpful comments, suggestions and help. This work was supported
475 by the ARC Future Fellowship program (FT100100443 to Meissner), the Australian-
476 American Fulbright Commission to Bralower, the NSERC CREATE training program
477 in interdisciplinary climate science at the University of Victoria, the ARC Centre of Ex-
478 cellence for Climate System Science, and the US National Science Foundation (EAR 06-
479 28394 to Bralower). TDJ acknowledges support from a Royal Dorothy Hodgkin Fellowship.
480 We are grateful for an award under the Merit Allocation Scheme on the NCI National
481 Facility at the ANU.

References

- 482 Abbot, D. S., and E. Tziperman (2009), Controls on the activation and strength of a
483 high-latitude convective cloud feedback, *Journal of Atmospheric Sciences*, *66*, 519–529.
- 484 Archer, D. (1996), A data-driven model of the global calcite lysocline, *Global Biogeo-*
485 *chemical Cycles*, *10*(3), 511–526.
- 486 Bains, S., R. M. Corfield, and R. D. Norris (1999), Mechanisms of climate warming at
487 the end of the Paleocene, *Science*, *285*(5428), 724–727.
- 488 Bice, K. L., and J. Marotzke (2001), Numerical evidence against reversed thermohaline
489 circulation in the warm Paleocene/Eocene ocean, *Journal of Geophysical Research*,

- Bralower, T. J. (2002), Evidence of surface water oligotrophy during the Paleocene-Eocene thermal maximum: Nannofossil assemblage data from Ocean Drilling Program Site 690, Maud Rise, Weddell Sea, *Paleoceanography*, *17*(2), 13:1–12.
- Bralower, T. J., J. C. Zachos, E. Thomas, M. Parrow, C. K. Paull, D. C. Kelly, I. Premoli Silva, W. V. Sliter, and K. C. Lohmann (1995), Late Paleocene to Eocene paleoceanography of the equatorial Pacific Ocean: Stable isotopes recorded at Ocean Drilling Program Site 865, Allison Guyot, *Paleoceanography*, *10*(4), 841–865.
- Cao, L., et al. (2009), The role of ocean transport in the uptake of anthropogenic CO₂, *Biogeosciences*, *6*(3), 375–390.
- Chun, C. O. J., M. L. Delaney, and J. C. Zachos (2010), Paleoredox changes across the Paleocene-Eocene thermal maximum, Walvis Ridge (ODP Sites 1262, 1263, and 1266): Evidence from Mn and U enrichment factors, *Paleoceanography*, *25*(4), PA4202.
- Colosimo, A. B., T. J. Bralower, and J. C. Zachos (2006), *Proc. ODP, Sci. Results*, chap. Evidence for lysocline shoaling at the Paleocene Eocene Thermal Maximum on Shatsky Rise, Northwest Pacific, ODP.
- Crouch, E. M., C. Heilmann-Clausen, H. Brinkhuis, H. E. G. Morgans, K. M. Rogers, H. Egger, and B. Schmitz (2001), Global dinoflagellate event associated with the late Paleocene thermal maximum, *Geology*, *29*(4), 315–318.
- Cui, Y., L. R. Kump, A. J. Ridgwell, A. J. Charles, C. K. Junium, A. F. Diefendorf, K. H. Freeman, N. M. Urban, and I. C. Harding (2011), Slow release of fossil carbon during the Palaeocene-Eocene Thermal Maximum, *Nature Geoscience*, *4*, 481–485.

512 Dickens, G. R., J. R. O’Neil, D. K. Rea, and R. M. Owen (1995), Dissociation of
513 oceanic methane hydrate as a cause of the carbon isotope excursion at the end of the
514 Paleocene, *Paleoceanography*, *10*(6), 965–971.

515 Dickens, G. R., M. M. Castillo, and J. C. G. Walker (1997), A blast of gas in the latest
516 Paleocene: Simulating first-order effects of massive dissociation of oceanic methane
517 hydrate, *Geology*, *25*(3), 259–262.

518 Dunkley Jones, T., D. J. Lunt, D. N. Schmidt, A. Ridgwell, A. Sluijs, P. J. Valdes, and
519 M. Maslin (2013), Climate model and proxy data constraints on ocean warming across
520 the Paleocene-Eocene Thermal Maximum, *Earth-Science Reviews*, *125*, 123–145.

521 Eby, M., K. Zickfeld, A. Montenegro, D. Archer, K. J. Meissner, and A. J. Weaver
522 (2009), Lifetime of anthropogenic climate change: Millennial time-scales of potential
523 CO₂ and surface temperature perturbations, *Journal of Climate*, *22*, 2501–2511.

524 Eppley, R. W. (1972), Temperature and phytoplankton growth in the sea, *Fishery Bul-*
525 *letin*, *70*(4), 1063–1085.

526 Evans, D., and W. Müller (2012), Deep time foraminifera Mg/Ca paleothermometry:
527 Nonlinear correction for secular change in seawater Mg/Ca, *Paleoceanography*, *27*,
528 PA4205.

529 Fyke, J., and M. Eby (2012), Comment on “Climate sensitivity estimated from temper-
530 ature reconstructions of the Last Glacial Maximum”, *Science*, *337*(1294).

531 Gehlen, M., R. Gangstø, B. Schneider, L. Bopp, O. Aumont, and C. Etche (2007), The
532 fate of pelagic CaCO₃ production in a high CO₂ ocean: A model study, *Biogeosciences*,
533 *4*(4), 505–519.

534 Goodwin, P., and A. Ridgwell (2010), Ocean-atmosphere partitioning of anthro-
535 pogenic carbon dioxide on multimillennial timescales, *Global Biogeochemical Cycles*,
536 *24*, GB2014.

537 Goodwin, P., R. G. Williams, A. Ridgwell, and M. J. Follows (2009), Climate sensitivity
538 to the carbon cycle modulated by past and future changes in ocean chemistry, *Nature*
539 *Geoscience*, *2*, 145–150.

540 Harris, A. D., K. G. Miller, J. V. Browning, P. J. Sugarman, R. K. Olsson, B. S. Cramer,
541 and J. D. Wright (2010), Integrated stratigraphic studies of Paleocene-lowermost
542 Eocene sequences, New Jersey Coastal Plain: Evidence for glacioeustatic control,
543 *Paleoceanography*, p. PA3211.

544 Heinemann, M., J. H. Jungclaus, and J. Marotzke (2009), Warm Paleocene/Eocene
545 climate as simulated in ECHAM5/MPI-OM, *Climate of the Past*, *5*, 785–802.

546 Hilting, A. K., L. R. Kump, and T. J. Bralower (2008), Variations in the oceanic vertical
547 carbon isotope gradient and their implications for the Paleocene-Eocene biological
548 pump, *Paleoceanography*, *23*, PA3222.

549 Hollis, C. J., et al. (2012), Early Paleogene temperature history of the Southwest Pacific
550 Ocean: reconciling proxies and models, *Earth and Planetary Science Letters*, *349-350*,
551 53–66.

552 Horita, J., H. Zimmermann, and H. D. Holland (2002), Chemical evolution of seawater
553 during the Phanerozoic: Implications from the record of marine evaporites, *Geochimica*
554 *and Cosmochimica Acta*, *66*(21), 3733–3756.

555 Huber, M. (2008), A hotter Greenhouse?, *Science*, *321*(5887), 353–354.

Huber, M., and R. Caballero (2011), The early Eocene equable climate problem revisited, *Climate of the Past*, 7, 603–633.

Kelly, D. C., T. J. Bralower, J. C. Zachos, I. Premoli Silva, and E. Thomas (1996), Rapid diversification of planktonic foraminifera in the tropical Pacific (ODP Site 865) during the late Paleocene thermal maximum, *Geology*, 24(5), 423–426.

Kennett, J. P., and L. D. Stott (1991), Abrupt deep-sea warming, palaeoceanographic changes and benthic extinctions at the end of the Palaeocene, *Nature*, 353, 225–229.

Kiehl, J. T., and C. A. Shields (2013), Sensitivity of the Paleocene-Eocene Thermal Maximum climate to cloud properties, *Philosophical Transactions of The Royal Society A*, 371(2001), 20130093.

Kim, J.-H., J. v. d. Meer, S. Schouten, P. Helmke, V. Willmott, F. Sangiorgi, N. Koç, E. C. Hopmans, and J. S. S. Damsté (2010), New indices and calibrations derived from the distribution of crenarchaeal isoprenoid tetraether lipids: Implications for past sea surface temperature reconstructions, *Geochimica et Cosmochimica Acta*, 74(16), 4639–4654.

Kim, S.-T., and J. R. O’Neil (1997), Equilibrium and nonequilibrium oxygen isotope effects in synthetic carbonates, *Geochimica et Cosmochimica Acta*, 61(16), 3461–3475.

Kozdon, R., D. C. Kelly, K. Kitajima, A. Strickland, J. H. Fournelle, and J. W. Valley (2013), In situ $\delta^{18}\text{O}$ and Mg/Ca analyses of diagenetic and planktic foraminiferal calcite preserved in a deep-sea record of the Paleocene-Eocene thermal maximum, *Paleoceanography*, 28(3), 517–528.

577 Kurtz, A. C., L. R. Kump, M. A. Arthur, J. C. Zachos, and A. Paytan (2003), Early
578 Cenozoic decoupling of the global carbon and sulphur cycles, *Paleoceanography*, *18*(4),
579 14:1–14.

580 Lear, C. H., Y. Rosenthal, and N. Slowey (2002), Benthic foraminiferal Mg/Ca- pa-
581 leothermometry: a revised core-top calibration, *Geochimica et Cosmochimica Acta*,
582 *66*(19), 3375–3387.

583 Lenton, T. M., and C. Britton (2006), Enhanced carbonate and silicate weathering
584 accelerates recovery from fossil fuel CO₂ perturbations, *Global Biogeochemical Cycles*,
585 *20*(3).

586 Lowenstein, T. K., M. N. Timofeeff, S. T. Brennan, L. A. Hardie, and R. V. Demicco
587 (2001), Oscillations in Phanerozoic seawater chemistry: Evidence from fluid inclu-
588 sions, *Science*, *294*, 1086–1088.

589 Lunt, D. J., A. M. Haywood, G. A. Schmidt, U. Salzmann, P. J. Valdes, and H. J.
590 Dowsett (2010), Earth system sensitivity inferred from Pliocene modelling and data,
591 *Nature Geoscience*, *3*, 60–64.

592 Lunt, D. J., et al. (2012), A model-data comparison for a multi-model ensemble of early
593 Eocene atmosphere-ocean simulations: EoMIP, *Climate of the Past*, *8*, 1229–1273.

594 Matthews, H. D., A. J. Weaver, and K. J. Meissner (2005), Terrestrial carbon cycle
595 dynamics under recent and future climate change, *Journal of Climate*, *18*, 1609–1628.

596 McInerney, F. A., and S. L. Wing (2011), The Paleocene-Eocene Thermal Maximum: A
597 perturbation of carbon cycle, climate, and biosphere with implications for the future,
598 *Annual Review of Earth and Planetary Sciences*, *39*, 489–516.

599 Meissner, K. J., A. J. Weaver, H. D. Matthews, and P. M. Cox (2003), The role of land
600 surface dynamics in glacial inception: a study with the UVic Earth System Model,
601 *Climate Dynamics*, *21*, 515 – 537.

602 Meissner, K. J., M. Eby, A. J. Weaver, and O. A. Saenko (2008), CO₂ threshold for
603 millennial-scale oscillations in the climate system: implications for global warming
604 scenarios, *Climate Dynamics*, *30*, 161–174.

605 Meissner, K. J., B. I. McNeil, M. Eby, and E. C. Wiebe (2012), The importance of the
606 terrestrial weathering feedback for multi-millennial coral reef habitat recovery, *Global*
607 *Biogeochemical Cycles*, *26*(GB3017).

608 Murphy, B. H., K. A. Farley, and J. C. Zachos (2010), An extraterrestrial ³He-based
609 timescale for the Paleocene-Eocene thermal maximum (PETM) from Walvis Ridge,
610 IODP Site 1266, *Geochimica et Cosmochimica Acta*, *74*(17), 5098–5108.

611 Pacanowski, R. C. (1995), MOM 2 Documentation, User’s Guide and Reference Man-
612 ual, *Tech. Rep. 3*, GFDL Ocean Group, Geophysical Fluid Dynamics Laboratory,
613 Princeton, USA.

614 Pagani, M., N. Pedentchouk, M. Huber, A. Sluijs, S. Schouten, H. Brinkhuis, J. S.
615 Sinninghe Damsté, G. R. Dickens, and the Expedition 302 Scientists (2006a), Arc-
616 tic hydrology during global warming at the Palaeocene Eocene thermal maximum,
617 *Nature*, *442*, 671–675.

618 Pagani, M., K. Caldeira, D. Archer, and J. C. Zachos (2006b), An ancient carbon
619 mystery, *Science*, *314*(5805), 1556–1557.

620 Pagani, M., Z. Liu, J. LaRiviere, and A. C. Ravelo (2010), High Earth-system cli-
 621 mate sensitivity determined from Pliocene carbon dioxide concentrations, *Nature Geo-*
 622 *science*, *3*, 27–30.

623 Pälike, C., M. L. Delaney, and J. C. Zachos (2014), Deep-sea redox across the Paleocene-
 624 Eocene thermal maximum, *Geochemistry, Geophysics, Geosystems*, *15*(4), 1038–1053.

625 Panchuk, K., A. Ridgwell, and L. R. Kump (2008), Sedimentary response to Paleocene-
 626 Eocene Thermal Maximum carbon release: A model-data comparison, *Geology*, *36*(4),
 627 315–318.

628 Panchuk, K. M. (2007), Investigating the Paleocene-Eocene carbon-cycle perturbation:
 629 An Earth System Model Approach, Ph.D. thesis, The Pennsylvania State University.

630 Pearson, P., and M. R. Palmer (2000), Atmospheric carbon dioxide concentrations over
 631 the past 60 million years, *Nature*, *406*, 695–699.

632 Pearson, P., P. Ditchfield, J. Singano, K. Harcourt-Brown, C. Nicholas, R. Olsson,
 633 N. Shackleton, and M. Hall (2001), Warm tropical sea surface temperatures in the
 634 Late Cretaceous and Eocene epochs, *Nature*, *413*(6855), 481–487.

635 Ridgwell, A., and D. N. Schmidt (2010), Past constraints on the vulnerability of marine
 636 calcifiers to massive carbon dioxide release, *Nature Geoscience*, *3*, 196–200.

637 Ridgwell, A., I. Zondervan, J. C. Hargreaves, J. Bijma, and T. M. Lenton (2007),
 638 Assessing the potential long-term increase of oceanic fossil fuel CO₂ uptake due to
 639 CO₂-calcification feedback, *Biogeosciences*, *4*, 481–492.

640 Rohling, E. J., et al. (2013), Making sense of palaeoclimate sensitivity, *Nature*, *491*,
 641 683–691.

642 Royer, D. N., S. L. Wing, D. J. Beerling, D. W. Jolley, P. L. Koch, L. J. Hickey, and R. A.
643 Berner (2001), Paleobotanical evidence for near present-day levels of atmospheric CO₂
644 during part of the Tertiary, *Science*, *292*, 2310–2313.

645 Sagoo, N., P. Valdes, R. Flecker, and L. J. Gregoire (2013), The early Eocene equable
646 climate problem: can perturbations of the climate model parameters identify possible
647 solutions?, *Philosophical Transactions of the Royal Society A*, *371*.

648 Schartau, M., and A. Oschlies (2003), Simultaneous data-based optimization of a 1D-
649 ecosystem model at three locations in the North Atlantic Ocean: Part 2. Standing
650 stocks and nitrogen fluxes, *Journal of Marine Research*, *61*(6), 795–821.

651 Schmittner, A., A. Oschlies, H. D. Matthews, and E. D. Galbraith (2008), Future
652 changes in climate, ocean circulation, ecosystems, and biogeochemical cycling sim-
653 ulated for a business-as-usual CO₂ emission scenario until year 4000 AD, *Global Bio-
654 geochemical Cycles*, *22*(1), GB1013.

655 Schmittner, A., N. M. Urban, J. D. Shakun, N. M. Mahowald, P. U. Clark, P. J. Bartlein,
656 A. C. Mix, and A. Rosell-Melé (2011), Climate sensitivity estimated from temperature
657 reconstructions of the Last Glacial Maximum, *Science*, *344*, 1385–1388.

658 Schubert, B. A., and A. H. Jahren (2013), Reconciliation of marine and terrestrial
659 carbon isotope excursions based on changing atmospheric CO₂ levels, *Nature Com-
660 munications*, *4*, 1653–6.

661 Sewall, J., and L. Sloan (2004), Less ice, less tilt, less chill: The influence of a season-
662 ally ice-free Arctic Ocean and reduced obliquity on early Paleogene climate, *Geology*,
663 *32*(6), 477–480.

664 Sijp, W. P., M. H. England, and M. Huber (2011), Effect of the deepening of the Tasman
665 Gateway on the global ocean, *Paleoceanography*, 26(PA4207).

666 Sloan, L., and D. Pollard (1998), A high latitude warming mechanism in an ancient
667 greenhouse world, *Geophysical Research Letters*, 25(18), 3517–3520.

668 Sloan, L. C., and E. J. Barron (1990), “Equable” climates during Earth history?, *Geol-*
669 *ogy*, 18, 489–492.

670 Sloan, L. C., and E. Thomas (1998), *Late Paleocene-early Eocene climatic and biotic*
671 *events in the marine and terrestrial records*, chap. General climate during the Late
672 Paleocene Thermal Maximum, pp. 138–157, University Press, New York: Columbia.

673 Sluijs, A., et al. (2006), Subtropical Arctic Ocean temperatures during the Palaeocene
674 Eocene thermal maximum, *Nature*, 441, 610–613.

675 Sluijs, A., G. J. Bowen, H. Brinkhuis, L. J. Lourens, and E. Thomas (2007a), *Deep-*
676 *time perspectives on climate change: Marrying the signal from computer models and*
677 *biological proxies*, chap. The Palaeocene-Eocene Thermal Maximum super greenhouse:
678 biotic and geochemical signatures, age models and mechanisms of global change, pp.
679 323–350, The Micropalaeontological Society Special Publication, London.

680 Sluijs, A., et al. (2007b), Environmental precursors to rapid light carbon injection at
681 the Palaeocene Eocene boundary, *Nature*, 450, 1218–1221.

682 Stocker, T. F., et al. (Eds.) (2013), *Climate Change 2013: The Physical Science Basis.*
683 *Contribution of Working Group I to the Fifth Assessment Report of the Intergovernmen-*
684 *tal Panel on Climate Change*, chap. Summary for Policymakers, Cambridge University
685 Press, Cambridge, United Kingdom and New York, NY, USA.

686 Taylor, K. W. R., M. Huber, C. J. Hollis, M. T. H. Sanchez, and R. D. Pancost (2013),
 687 Re-evaluating modern and Palaeogene GDGT distributions: Implications for SST
 688 reconstructions, *Global and Planetary Change*, *108*, 158–174.

689 Thomas, D. J., J. C. Zachos, T. J. Bralower, E. Thomas, and S. Bohaty (2002), Warming
 690 the fuel for the fire: Evidence for the thermal dissociation of methane hydrate during
 691 the Paleocene-Eocene thermal maximum, *Geology*, *30*(2), 1067–1070.

692 Thomas, D. J., T. J. Bralower, and C. E. Jones (2003), Neodymium isotopic reconstruc-
 693 tion of late Paleocene-early Eocene thermohaline circulation, *Earth and Planetary*
 694 *Science Letters*, *209*, 309–322.

695 Thomas, E. (1998), *Late Paleocene-early Eocene climatic and biotic events in the*
 696 *marine and terrestrial records*, chap. Biogeography of the Late Paleocene Benthic
 697 Foraminiferal Extinction, pp. 214–243, University Press, New York: Columbia.

698 Thomas, E., and N. J. Shackleton (1996), The late Paleocene benthic foraminiferal
 699 extinction and stable isotope anomalies, *Geol. Soc. Spec. Publ.*, *101*, 401–441.

700 Tyrrell, T., and R. E. Zeebe (2004), History of carbonate ion concentration over the
 701 last 100 million years, *Geochim. Cosmochim. Acta*, *68*(17), 3521–3530.

702 Valdes, P. (2011), Built for stability, *Nature Geoscience*, *4*, 414–416.

703 Waddell, L., and T. Moore (2008), Salinity of the Eocene Arctic Ocean from oxygen
 704 isotope analysis of fish bone carbonate, *Paleoceanography*, *23*(1), PA1S12.

705 Weaver, A. J., et al. (2001), The UVic Earth System Climate Model: Model description,
 706 climatology, and applications to past, present and future climates, *Atmos.-Ocean.*, *4*,
 707 361–428.

708 Weaver, A. J., M. Eby, M. Kienast, and O. A. Saenko (2007), Response of the Atlantic
709 meridional overturning circulation to increasing atmospheric CO₂: Sensitivity to mean
710 climate state, *Geophysical Research Letters*, *34*(5), L05,708.

711 Westerhold, T., U. Röhl, J. Laskar, I. Raffi, J. Bowles, L. J. Lourens, and J. C. Zachos
712 (2007), On the duration of magnetochrons C24r and C25n and the timing of early
713 Eocene global warming events: Implications from the Ocean Drilling Program Leg
714 208 Walvis Ridge depth transect, *Paleoceanography*, *22*, PA2201.

715 Wing, S. L., G. J. Harrington, F. A. Smith, J. I. Bloch, D. M. Boyer, and K. H. Freeman
716 (2005), Transient floral change and rapid global warming at the Paleocene-Eocene
717 boundary, *Science*, *310*(5750), 993–996.

718 Winguth, A. M. E., E. Thomas, and C. Winguth (2012), Global decline in ocean ventila-
719 tion, oxygenation, and productivity during the Paleocene-Eocene Thermal Maximum:
720 Implications for the benthic extinction, *Geology*, *40*(3), 263–266.

721 Wright, J. D., and M. F. Schaller (2013), Evidence for a rapid release of carbon at the
722 Paleocene-Eocene thermal maximum, *Proceedings of the National Academy of Sciences*
723 *of the United States of America*, *110*(40), 15,908–15,913.

724 Zachos, J. C., M. W. Wara, S. Bohaty, M. L. Delaney, M. R. Petrizzo, A. Brill, T. J.
725 Bralower, and I. Premoli-Silva (2003), A transient rise in tropical sea surface tempera-
726 ture during the Paleocene-Eocene thermal maximum, *Science*, *302*(5650), 1551–1554.

727 Zachos, J. C., et al. (2005), Rapid acidification of the ocean during the Paleocene-Eocene
728 Thermal Maximum, *Science*, *308*(5728), 1611–1615.

729 Zachos, J. C., S. M. Bohaty, C. M. John, H. McCarren, D. C. Kelly, and T. Nielsen
730 (2007), The Paleocene-Eocene carbon isotope excursion: Constraints from individual
731 shell planktonic foraminifer records, *Royal Society Phil. Trans. A*, *365*, 1829–1842.

732 Zeebe, R. E., and J. C. Zachos (2013), Long-term legacy of massive carbon input to
733 the Earth system: Anthropocene vs. Eocene, *Philosophical Transactions of the Royal*
734 *Society A*, *371* (2001).

735 Zeebe, R. E., J. C. Zachos, K. Caldeira, and T. Tyrrell (2008), Oceans: Carbon emissions
736 and acidification, *Science*, *321* (5885), 51–52.

737 Zeebe, R. E., J. C. Zachos, and G. R. Dickens (2009), Carbon dioxide forcing alone insuf-
738 ficient to explain Palaeocene-Eocene Thermal Maximum warming, *Nature Geoscience*,
739 *2*, 576–580.

740 Zeebe, R. E., G. R. Dickens, A. Ridgwell, A. Sluijs, and E. Thomas (2014), Onset of
741 carbon isotope excursion at the Paleocene-Eocene thermal maximum took millennia,
742 not 13 years, *Proc. Natl. Acad. Sci.*, *111* (12), 201321,177–E1063.

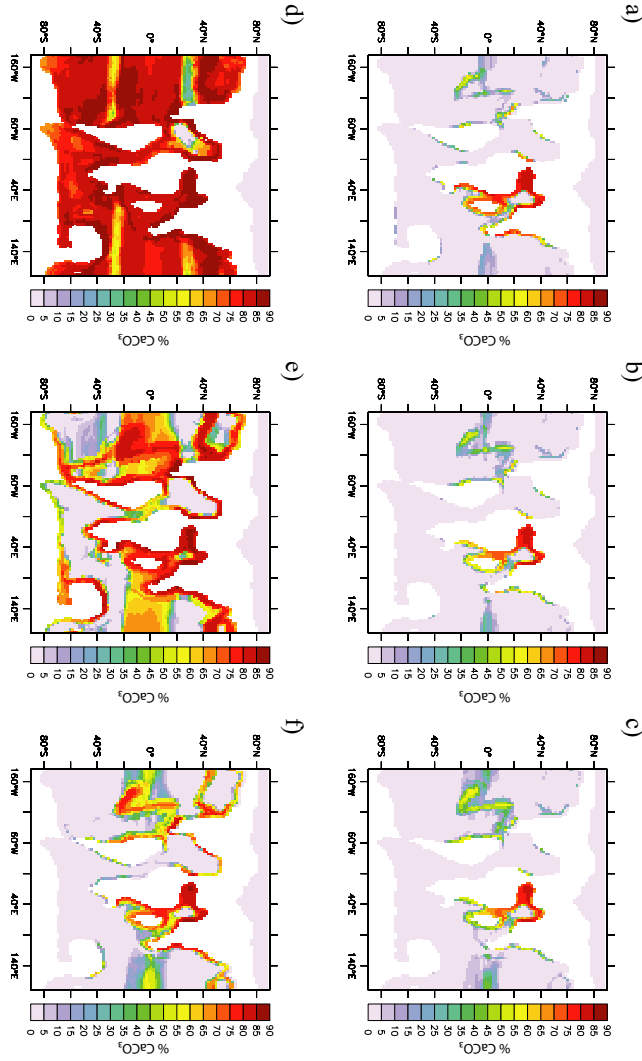


Figure 1. Annual mean percent dry weight CaCO_3 for the six warmer equilibrium simulations; (a) 840, (b) 1680, (c) 2520, (d) 1680_Alk2, (e) 1680_Alk15, (f) 1680_Alk12.

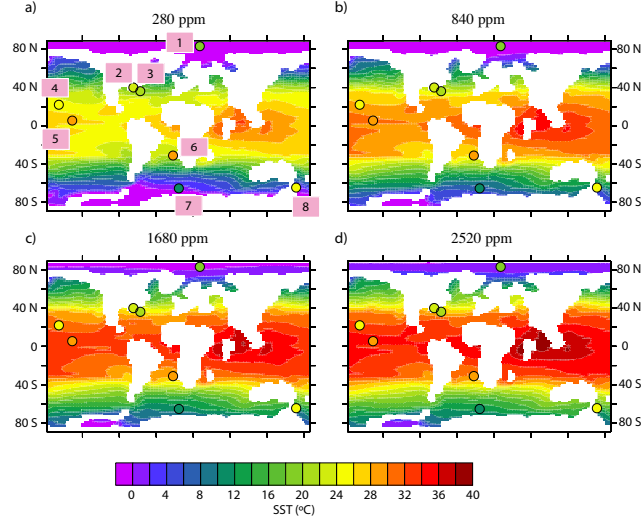


Figure 2. Annual mean sea surface temperatures in $^{\circ}\text{C}$ for the four equilibrium simulations. Also shown are pre-PETM SST reconstructions from proxy data compiled by *Dunkley Jones et al.* [2013]; for sites with several reconstructions of pre-PETM SST, we have plotted the median value. Sites are labeled in (a) as follows: [1] Integrated Ocean Drilling Program (IODP) Leg 302 ACEX core, [2] Bass River, [3] Wilson Lake, [4] Ocean Drilling Program (ODP) Sites 1209, [5] 865, [7] 690, and [8] 1172, and [6] Deep Sea Drilling Project Site 527. Note that [2] and [3] are shown shifted slightly apart for ease of viewing.

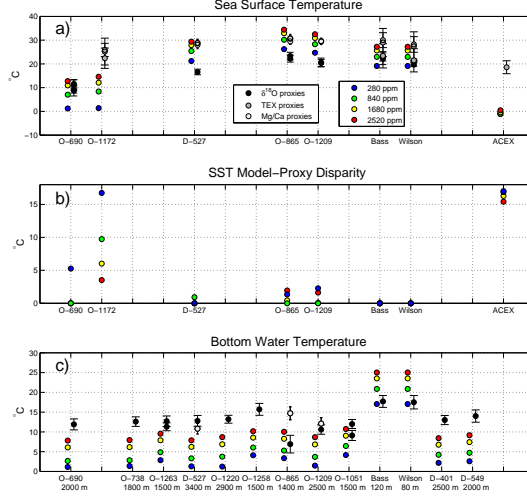


Figure 3. Annual mean sea surface ocean temperatures (a) and ocean bottom temperatures (c) in °C for the four equilibrium simulations compared to pre-PETM proxy data compiled by *Dunkley Jones et al.* [2013]. Model-data disparity (calculation described in the text) for each simulation and site is shown in (b). Note that in (c) the depth of ODP 1258 is taken at 1500 m (rather than 2500 m as in *Dunkley Jones et al.* [2013]), which is the maximum depth of the ocean model at that location.

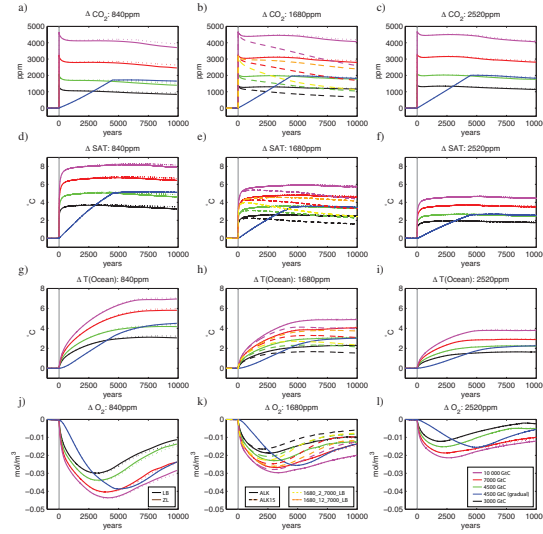


Figure 4. Annual mean model results for all transient simulations. Columns (left to right) show simulations initialised with 840, 1680, and 2520 ppm CO_2 ; rows (top to bottom) show atmospheric CO_2 concentration anomalies in ppm, global mean surface atmospheric temperature (SAT) anomalies, global mean ocean temperature anomalies and global mean oceanic oxygen concentrations. Simulations with carbon pulses of 3000, 4500, 7000, and 10 000 GtC are plotted in black, green, red, and pink respectively; gradual release simulations (1 GtC/year for 4500 years) are shown in blue. Simulations with the LB and ZL weathering schemes are plotted with solid and dotted lines respectively. Simulations initialized with 1.5 times present day alkalinity are shown in dashed lines (colours corresponding to magnitude of carbon pulse). 1680_12_7000_LB and 1680_2_7000_LB are shown in orange and yellow dashed lines respectively. Light grey vertical lines show the time of carbon release.

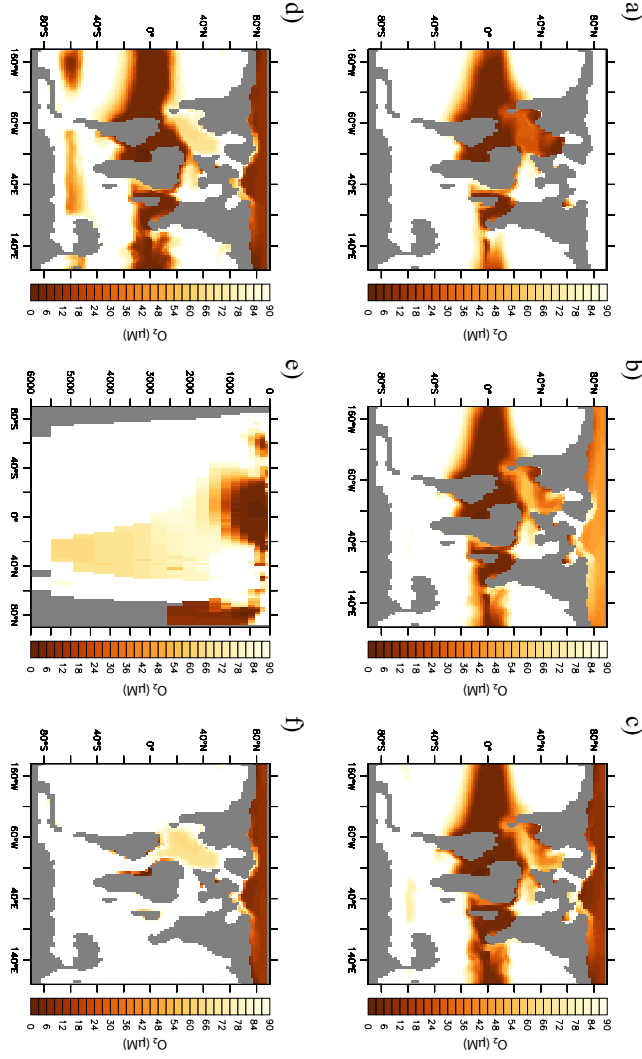


Figure 5. Annual mean minimum oxygen concentrations in the water column in μM (10^{-3}mol/m^3). Only values below $90 \mu\text{M}$ are shown. Upper panels show equilibrium simulations: (a) 840, (b) 1680, (c) 2520. Lower panels show simulation 2520_10000_LB at year 2600 after the pulse: (d) vertical minimum concentration, (e) zonal minimum concentration, (f) bottom water oxygen concentrations.

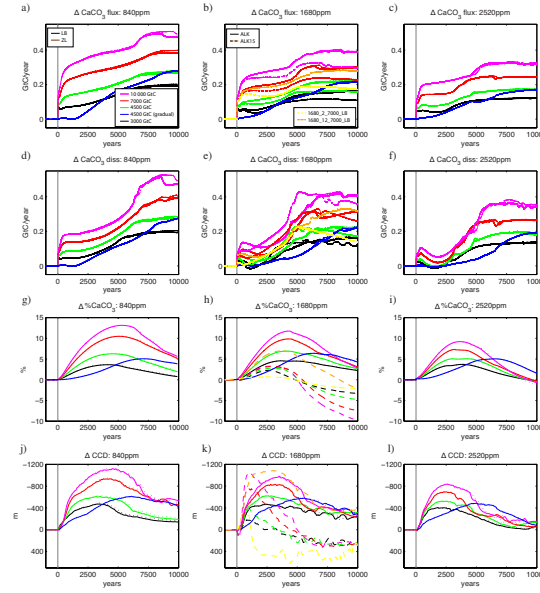


Figure 6. Annual and global mean sediment model results for all transient simulations. Columns (left to right) show simulations initialised with 840, 1680, and 2520 ppm CO_2 ; rows (top to bottom) show anomalies of global mean downward flux of calcite into the sediments in GtC/year, dissolution of calcite in sediments (GtC/year), calcite pore layer portion (in %), and calcite compensation depth (defined here as the mean depth of grid boxes with less than 10% dry weight CaCO_3 ; negative values designate a shoaling of this metric). Simulations with carbon pulses of 3000, 4500, 7000, and 10000 GtC are plotted in black, green, red, and pink respectively; gradual release simulations (1 GtC/year for 4500 years) are shown in blue. Simulations with the LB and ZL weathering schemes are plotted with solid and dotted lines respectively. Simulations initialized with 1.5 times present day alkalinity are shown in dashed lines (colours corresponding to magnitude of carbon pulse). 1680.12-7000_LB and 1680.2-7000_LB are shown in orange and yellow dashed lines respectively. Light grey vertical lines show the time of carbon release.

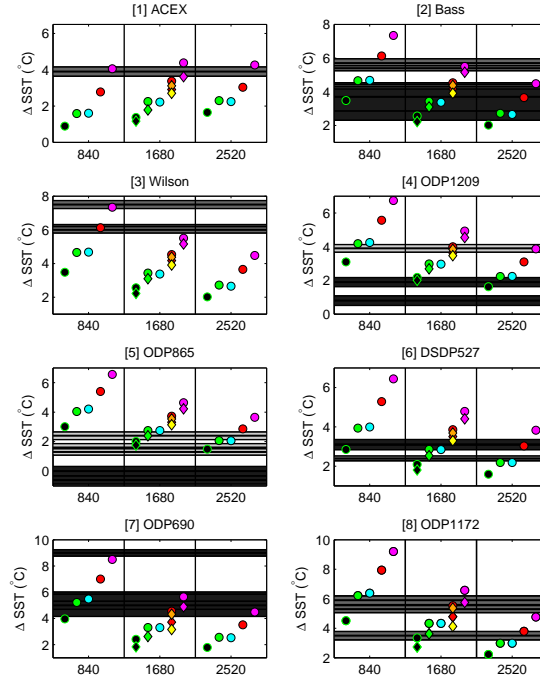


Figure 7. Maximum temperature anomaly for sea surface temperatures (ACEX, Bass, Wilson, Sites 1209, 865, 527, 690 and 1172). Each panel is split into 3 columns for simulations starting at 840 ppm (left), 1680 ppm (middle) and 2520 ppm (right). Carbon releases of 3000, 4500, 7000, and 10000 GtC are plotted in black, green, red, and pink respectively; gradual release simulations (1 GtC/year for 4500 years) are shown in blue. Simulations with present-day and 1.5 times present-day alkalinity are plotted with circles and diamonds respectively. Orange and yellow diamonds stand for simulations 1680_12_7000LB and 16800_2_7000LB respectively. Horizontal bars in light (Mg/Ca), medium (TEX), and dark (δO^{18}) grey show proxy reconstructions with standard error.

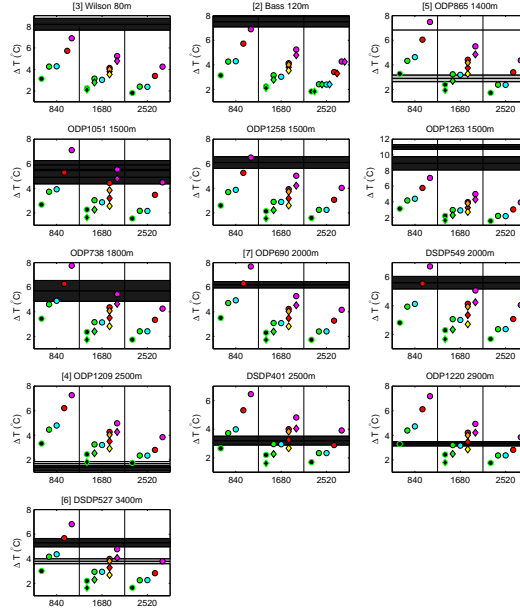


Figure 8. Maximum temperature anomaly for bottom temperatures. Each panel is split into 3 columns for simulations starting at 840 ppm (left), 1680 ppm (middle) and 2520 ppm (right). Carbon releases of 3000, 4500, 7000, and 10 000 GtC are plotted in black, green, red, and pink respectively; gradual release simulations (1 GtC/year for 4500 years) are shown in blue. Simulations with present-day and 1.5 times present-day alkalinity are plotted with circles and diamonds respectively. Simulations 1680_12_7000_LB and 16800_2_7000_LB are plotted with orange and yellow diamonds respectively. Horizontal bars in light (Mg/Ca), medium (TEX), and dark (δO^{18}) grey show proxy reconstructions with standard error. Note that the depth of ODP 1258 is taken at 1500 m (rather than 2500 m as in *Dunkley Jones et al.* [2013]), which is the maximum depth of the ocean model at that location.

Table 1. List of Simulations. LB and ZL denote the weathering scheme used (see text and*Meissner et al.* [2012])

Control Simulation	Transient Pulse		Transient Gradual Release (1 Pg C /year)	
	Emission (Pg C)	Name	Emission (Pg C)	Name
280	-	-	-	-
840	3000	840_3000_LB 840_3000_ZL	4500	840_4500G_LB 840_4500G_ZL
	4500	840_4500_LB 840_4500_ZL		
	7000	840_7000_LB 840_7000_ZL		
	10000	840_10000_LB 840_10000_ZL		
1680	3000	1680_3000_LB 1680_3000_ZL	4500	1680_4500G_LB 1680_4500G_ZL
	4500	1680_4500_LB 1680_4500_ZL		
	7000	1680_7000_LB 1680_7000_ZL		
	10000	1680_10000_LB 1680_10000_ZL		
1680_Alk12	7000	1680_12_7000_LB	-	-
1680_Alk15	3000	1680_15_3000_LB	-	-
	4500	1680_15_4500_LB		
	7000	1680_15_7000_LB		
	10000	1680_15_10000_LB		
1680_Alk2	7000	1680_2_7000_LB	-	-
2520	3000	2520_3000_LB 2520_3000_ZL	4500	2520_4500G_LB 2520_4500G_ZL
	4500	2520_4500_LB 2520_4500_ZL		
	7000	2520_7000_LB 2520_7000_ZL		
	10000	2520_10000_LB 2520_10000_ZL		